Transition from many domain to single domain martensite morphology in small-scale shape memory alloys

Citation: Ueland, Stian M., and Christopher A. Schuh. "Transition from Many Domain to Single Domain Martensite Morphology in Small-Scale Shape Memory Alloys." Acta Materialia 61, no. 15 (September 2013): 5618–5625.

As Published: http://dx.doi.org/10.1016/j.actamat.2013.06.003

Publisher: Elsevier

Persistent URL: http://hdl.handle.net/1721.1/102382

Version: Author's final manuscript: final author's manuscript post peer review, without publisher's formatting or copy editing

Transition from many-domain to single-domain martensite transformation morphology in small scale shape memory alloys

Stian M. Ueland, Christopher A. Schuh[1]

Department of Materials Science and Engineering, Massachusetts Institute of Technology,
77 Massachusetts Avenue, Cambridge, MA 02139, USA

The morphology of the martensitic transformation during a superelastic cycle is studied by *in situ* scanning electron microscopy deformation experiments in microwires of Cu-Zn-Al. The diameters of the wires studied (from 21 to 136 μm) span the range where significant size effects upon transformation hysteresis have been observed. In larger wires the transformation is accommodated by the continual nucleation of many new martensite plates that grow and eventually coalesce with their neighbors. In the small wires a single martensite plate nucleates at the start of the transformation and then proceeds to grow in a monolithic fashion; the wire transforms by the smooth axial propagation of a single interface. The transition from many- to single-domain transformation is gradual with wire diameter, and based upon the scaling of domain density with sample size, we attribute it to a crossover from bulk to surface-obstacle control of the transformation front propagation. This observation also sheds light upon reported size effects in energy dissipation in shape memory alloys.

Keywords: *In situ*; Phase morphology; Martensitic transformation; Size effect; Nucleation and growth

[1] Corresponding author: Email address: schuh@mit.edu (C.A Schuh).

1. Introduction

Several aspects of the reversible martensitic phase transformation in shape memory alloys (SMAs) have been found to depend on sample size [1-9]; their response changes when a 'characteristic length' related to the mechanics of the phase transformation interacts with a sample size parameter. For example, when the characteristic size (e.g. grain size or pillar diameter) is decreased into the nanometer range, a loss of superelasticity and shape memory has been reported for Ni-Ti, such as for a grain size below ~50 nm [1, 10, 11]. Similarly, for Fe-Ni powders subjected to quenching through the transformation temperature, the probability of martensite formation decreases with decreasing particle diameter in the micron range [12]. Other properties, though, are enhanced in small scale samples such as in Ni-Mn-Ga where the magnetic field-induced strain increases dramatically in highly porous foams [13].

Recently, a different type of size effect was reported in Cu-based SMA microwires with a bamboo grain structure [14-16]. For wires of both Cu-Al-Ni and Cu-Zn-Al the transformation hysteresis was observed to increase as the wire diameter decreased from ~100 to ~20 μm [14]. In line with these results, microcompression studies on Cu-Al-Ni single crystalline pillars with diameters of ~1 μm show a much larger superelastic hysteresis than their bulk counterparts [17-20]; smaller samples dissipate more energy per unit volume than larger samples. The energy dissipation in SMAs, manifested by the hysteresis, is related to the movement of the austenite/martensite interface where energy is dissipated in the form of frictional work spent on overcoming resistance to interface motion [21, 22].

For Cu-Al-Ni microwires, the size effect has been attributed to enhanced frictional energy dissipation at the free surfaces in smaller wires when the martensite plates

propagate along the sample axis [16]. Nonlocal continuum modeling of Cu-Al-Ni nanopillars, furthermore, related the size effect to the non-uniform evolution of the phase transformation [23]. However, the above works offered these explanations for the size effect as hypotheses, which are strongly related to an assumed morphology of the phase transformation, without the benefit of any direct observations that speak to the morphological evolution of martensite in any SMA in this size range (~5 - 500 μm).

At the millimeter scale, the nucleation and propagation of martensite has been studied by various *in situ* techniques such as optical microscopy (OM) [24-28], digital image correlation [29-31] and thermal observations with an infrared camera [32, 33]. In large single crystals loaded uniaxially the evolution of martensite plates seems to be one of nucleation, growth (both perpendicular and parallel to the loading axis) and coalescence of plates [24, 25]. The transformation also appears to be hierarchical, meaning that larger macroscopic bands grow by the nucleation of a myriad of smaller plates at the transformation front [24, 25, 34, 35]. At the nanometer size scale, also, SMAs have been studied *in situ* using transmission electron microscopy (TEM), for example to investigate the suppression of phase transformation indicated by ex situ mechanical measurements [36]. The technique has also been employed to study the morphological evolution of martensite plates as they nucleate and grow and how this evolution is affected by dislocations [37, 38] grain boundaries [39] and precipitates [40-42]. Lastly, *in situ* studies have been used to study interfaces [43], determining selection rules for stress-induced martensite phases and variants [44-47] and observing dislocation substructure evolution during cycling [48-51].

In the size range between what can be captured with TEM (nm) and OM (mm), however, there is a general lack of *in situ* studies on the morphology and kinematics of the martensitic transformation in SMAs. Furthermore, free surface effects, although ubiquitous, are often ignored in TEM studies and are expected to play only a minor role in millimeter size samples, and thus remain essentially unexplored in superelastic SMAs. This again connects to the array of size effects seen in samples with dimensions of a few to a few hundred μm, where surface effects may be significant but their role is speculative at present. The purpose of this paper is to start closing this gap, with a first *in situ* scanning electron microscopy (SEM) study of Cu-Zn-Al SMA microwires. The sample size range presented here span microscale diameters where a size effect has been observed, as well as larger diameters more typical of a conventional bulk specimen.

2. Methods and materials

The microwires used in this study were prepared using the Taylor liquid drawing technique [52, 53]. Solid alloy pieces of composition Cu–22.9%Zn–6.3%Al (wt.%) were placed in a closed-end aluminosilicate glass tube with 4 mm inner diameter and a working temperature of ~1250 °C. The inside of the tube was then subjected to low vacuum conditions and heated by an oxy-acetylene burner until the metal melted and the glass softened, at which point a glass capillary was drawn with the molten metal at its core. To promote grain growth into the stable bamboo structure, the as-drawn wires (still in the glass sheath) were annealed in an argon atmosphere for 3 h at 800 °C and water quenched. The glass coating was removed by immersion in ~10 % diluted aqueous hydrofluoric acid. *In situ* SEM deformation experiments were performed on five samples. The five wires were obtained with different draw speeds

yielding diameters ranging from 21 to 136 μm. Two wires (with diameters 21 and 116 μm) showing representative behavior will be presented in detail and will for simplicity be referred to as the fine wire and the coarser wire, respectively. Some wires are slightly tapered and the diameters are therefore average values. Dynamic scanning calorimetry (DSC) results, obtained at a rate of 10 °C·min^{-1}, are shown in Fig. 1. The transformation temperatures, as indicated in the plot, are observed to be $A_f \sim 25$, $A_s \sim 9$, $M_s \sim 8$ and $M_f \sim -6$°C (austenite finish and start, martensite start and finish, respectively).

The *in situ* tensile tests were performed at room temperature using a deformation stage (Gatan Microtest 200) inside of a scanning electron microscope (SEM). The wires were gently heated before mechanical testing to ensure single phase conditions (cf. Fig. 1). Epoxy was used to create grips at the wire ends to ensure sound mechanical contact. The wire surface was monitored *in situ* during the test and deformation was interrupted at regular intervals to obtain high quality images as the wire transformed. The strain rate was ~10^{-4} s^{-1}: no 'dynamic effects' (e.g. variant redistribution) were observed between deformation interruption and image capturing. All strains are inferred from the images and therefore represent 'local' strains in the photographed region. These local strains were measured between grain boundaries when they were observed within the field of view; a feature on the wire surface was used in cases where the imaged region contained only one grain boundary. The gauge lengths were 12 and 15 μm for the fine and coarser wires respectively.

3. Martensite morphology during a superelastic cycle

3.1 Martensite morphology in fine and coarser wires

The morphological evolution of martensite during a superelastic cycle at room temperature is shown in Fig. 2 for the coarse wire with a diameter of 116 μm. The panels in Fig. 2 focus on a single grain with a large aspect ratio of 4, bounded by grain boundaries on either side (marked by dashed red lines in the upper left panel); this is a typical oligocrystalline structure [14, 54]. The left column of Fig. 2 shows the sequence of events upon loading of this coarse wire. A local digital-image correlation-based measurement of the tensile strain level is noted next to each panel. As the wire is stretched martensite becomes visible as surface relief. In the successive panels of Fig. 2 we have enhanced the contrast of the martensite phase for visual clarity; raw images are made available as supplemental material online [55].

We see that the first plates are nucleated near the left grain boundary and that the transformation is further accommodated by the nucleation of new plates distributed along the length of the grain. These then also thicken until they communicate with their neighboring plates and coalesce into a single domain. In the last panel on the left the grain is almost fully transformed. The image sequence for the reverse transformation is shown on the right of Fig. 2, and proceeds by large martensite areas fragmenting into a myriad of thinner plates. Because the test temperature is very close to A_f, a few martensite plates are observed in the last panel of Fig. 2 resulting in a small residual strain of 0.1 %. The transformation evolution in Fig. 1 is qualitatively very similar to what is observed under *in situ* OM for bulk SMA samples [24, 25, 35], which, even under single-variant conditions is characterized by a large proliferation of separate domains followed by their coalescence, both on the forward and reverse transformations.

In Fig. 3 we show the complementary set of images for the same kind of test on the finer wire with diameter 21 μm. As in Fig. 2 we have enhanced the contrast of the martensite phase for visual clarity. The field of view shows a section of wire that comprises a single grain, except for one grain boundary located at the right side of the wire and denoted by a dashed red line in the first panel. The left column of Fig. 3 shows the image series upon loading, where the first two martensite plates that form are, like for the coarse wire, nucleated near a grain boundary. However, the subsequent kinematics of the transformation in this finer wire are strikingly different from those seen in Fig. 2 in the coarse wire. Instead of being accommodated by the continual nucleation and coalescence of new plates, the transformation now proceeds in a monolithic fashion; the wire transforms by the smooth axial propagation of a single interface. The unloading sequence for the wire is shown in the right-hand column of Fig. 3, where the reverse transformation is seen to mirror the forward transformation: the single martensite plate remains monolithic and shrinks from left to right as the load is reduced, and the large transformation strain of 9.5 % is almost fully recovered. Only a very thin plate, isolated between the grain boundary and the right end of the principal plate, does not transform back to austenite, which is reasonable since the test temperature is very close to A_f. This transformation pathway is again in stark contrast to that observed in the coarse wire where the reverse transformation also proceeded by domain fragmentation. The strain achieved in this wire is somewhat larger (9.5% as compared to 6.2%), being most likely an effect of local crystallographic orientation, which is uncontrolled for in these experiments.

In order to quantitatively compare the significance of nucleation and growth in the fine and coarser wires we measure the linear plate number density as shown in Fig. 4 against the transformed fraction (i.e., the instantaneous strain normalized by the

maximum strain at the end of the transformation). We see that for the fine wire two plates (within the field of view) are nucleated early in the test, and the fact that one of them grows is reflected by the long, horizontal shelf in the plot; strain (volume fraction) increases without requiring further domain nucleation. In other words, the high interface mobility renders further martensite plate nucleation unnecessary.

For the coarser wire, on the other hand, the evolution is quite different—strain is accumulated to a large extent by the continual nucleation of new phase domains. At medium strains, the process of coalescence begins to occur and gradually dominates beyond the peak in Fig. 4, where new plates are emerging at approximately the same rate as established ones coalesce, and the slope of the curve flattens out. As the maximum strain is approached, the plates coalesce and the curve dips. The reverse transformation is similar to the forward one except for the higher number of plates caused by the fragmenting of large plates.

3.2 Sample size dependencies on martensite plate density

In Fig. 5a we provide data for three more SMA wires in addition to the two pictured in Figs. 2-3, and plot the maximum number of martensite domains during superelastic tests, as well as the average number over the course of a cycle, as a function of the wire diameter, D. Although there is scatter in the data, a clear trend emerges across all of our tested wires, where smaller wires contain fewer domains per unit length as they transform. In other words, the finer the wire, the more domain growth relative to nucleation, and hence for the smallest wires we observe the single-domain transformation morphology in Fig. 3. For the coarser wires, on the other hand, growth is more difficult and hence multi-domain nucleation accommodates the strain. We believe that these differences in transformation kinematics, namely the transition from

multi-domain to single-domain transformation, are a sample size effect. The lines labeled ‘surface’ and ‘volume’, as well as Fig. 5b (which shows the data from Fig. 5a plotted on a per volume basis in stead of per length) will be discussed later in the text.

Although factors other than sample size, such as extremely low dislocation densities and temperature gradients have been shown to produce single interface transformations in large samples [56-58], these special conditions are not expected in the present experiments, and larger SMA samples generally exhibit phase morphology and evolution very similar to that seen in our large wire [24, 25, 35]. Furthermore, the two wires presented here were produced from the same initial pellet, given the same thermal treatment and preparation; they should have similar defect structures (although their sizes may sample defects differently—a point to which we shall shortly return). We can also rule out stress multiaxiality effects or end effects, as all of our images are taken far from the grips and show ~1-3 % of very long gauge sections; all wires experience the same uniaxial tensile stress state.

4. Obstacle density and morphology

After the first martensite plate has been formed, the wire has two options to accommodate further deformation: the initial plate can grow or new plates can nucleate in the austenite. Growth may be expected to be easier with increasing degree of crystal perfection [59]; if the interface is presented with obstacles, i.e., any type of crystal imperfection, growth will be more difficult [58]. For all of our wires, the martensite plates span the cross section, and the transformation front will encounter such obstacles as it traverses the length of the wire. If the material has an intrinsic volumetric number density of defects or obstacles, n_v, then the number of obstacles per unit length of interface traversal would be $\sim \frac{\pi}{4} \cdot D^2 \cdot n_v$. On the other hand, for

fine wires it has been proposed that surface defects may also be important obstacles to transformation front propagation [16], which would obey a different scaling with the number of obstacles per length going as $\sim \pi \cdot D \cdot n_s$ with n_s the areal number density of surface defects.

If transformation fronts are waylaid by obstacles, encouraging the nucleation of new domains, then, to first order the number of martensite domains observed in a specimen would be proportional to the number of obstacles. In this light, the data in Fig. 5a are now compared with the black lines representing linear (surface) and quadratic (volume) scaling with D as discussed above. The results are suggestive: the martensite domain density (per unit length) scales far more closely with D, as expected for surface-obstacle control, than with D^2 for volume-obstacle control.

The scaling of plate density with obstacles at the wire surface, as suggested by Fig. 5a, is in line with the size-dependent behavior in a related SMA, Cu-Al-Ni, studied by Chen and Schuh [16]. They related their observation of a size effect in superelastic hysteresis to the increased pinning of the transformation front at free surfaces; the cross-over from volume to surface dominated physics was shown to take place in wires with diameters around, or just below, 100 μm. Another example of size dependent behavior in SMAs is that of polycrystalline SMAs, where several alloy families show a decrease in M_s with decreasing grain size [60-65]. Interestingly, these effects also show little or no size dependence for large grains, but start to emerge for grain sizes below ~100 μm.

5. Size effects

5.1 Size effect in hysteresis

The above observations suggest that the sampling of defects, or obstacles, by the transformation front, changes with sample size, and this should be in principle related to some of the size effects previously reported in shape memory alloys. For example, we may re-examine the size effect on transformation hysteresis in light of the above discussion, because hysteresis is directly related to transformation obstacles [21, 66, 67]. During a thermoelastic martensitic transformation the moving interface has to perform an amount of frictional work related to the number and nature of the obstacles it meets [21, 67]. The energy dissipated as heat when the austenite-martensite interface bypasses these obstacles is reflected in the magnitude of the stress hysteresis [67]. As a first order model, the stress hysteresis magnitude, $\Delta\sigma$, is simply proportional to the obstacle number density, n, per unit volume of sample

$$\Delta\sigma = E_0 \cdot n \tag{1}$$

where E_0 is the energy dissipated per obstacle bypassed. Our previous observations about obstacle densities based on Fig. 5a can thus be used to explain a size effect on hysteresis, with one adjustment. The data in Fig. 5a are normalized per unit length of wire, but hysteresis is measured over the whole specimen volume; in Fig. 5b we replot the data of Fig. 5a on a per volume basis instead of per length. The volumetric densities of volume and surface obstacles are n_v and $\frac{4 \cdot n_s}{D}$ respectively. Furthermore, we can speculate that the surface and volume defects are of the same nature and from the same defect population, their position at the surface and in the interior being their only distinguishing trait. In that case $n_s \approx D_o \cdot n_v$, where D_o is a characteristic obstacle length scale. The volume and surface scalings are shown as black lines in Fig. 5b.

Although the smaller specimens transition from multi-domain to single-domain character (Fig. 5a), one can now better appreciate that this involves a higher overall volumetric density of domains (Fig. 5b). And with a higher density of domains, n, hysteresis rises according to Eq. 1, which can be rewritten using the obstacle density definitions above as:

$$\Delta\sigma = E_0 \cdot n_v(1 + \frac{4 \cdot D_o}{D}) \quad (2)$$

Here the leading term describes a volume-obstacle effect and the second term a surface-obstacle one. Owing to the 1/D dependence of the latter, we expect to see no size effect for samples sufficiently large, and a cross-over to a 1/D size scaling for small samples that are surface-obstacle dominated. In Fig. 6 we plot data for vertical hysteresis size of Cu-Zn-Al [15] and Cu-Al-Ni [16] wires as well as data for larger single crystalline Cu-based alloys [35, 68, 69] against wire diameter. The solid black line is Eq. 2 while the red lines represent the surface and volume terms plotted separately.

The free parameters are obtained by fitting to the data: $n_v = 6 \cdot 10^{13}$ m^{-3}, $D_o = 40$ μm and $E_0 = 1.1 \cdot 10^{-7}$ J. The match to the data is good, including a plateau of hysteresis for large samples and an increase that appears to reasonably follow a 1/D dependence for samples below about 100 μm. Furthermore, the fitting parameters seem physically reasonable; for example, we might compare the fitted obstacle density to that expected for point defects: the equilibrium vacancy concentration in quenched samples should lie between that at room temperature and at the annealing temperature, which in Cu are ~10^6 and ~10^{19} m^{-3}, respectively. As a second comparison, a typical dislocation density of ~10^{11} m^{-2} divided by a typical burgers vector of ~10^{-10} m yields a volumetric density of ~10^{21} m^{-3}. Whereas the fitted

obstacle density found from Eq. (2) (~10^{13} m^{-3}) is in the middle of the range of point defect concentrations, it is far smaller than the dislocation density. This suggests that the "obstacles" to martensitic transformation are rarer than dislocations, and may be, e.g., dislocation junctions or point defects.

5.2 Starvation of obstacles

In the preceding sections we have related martensite transformation morphology to the ease of domain growth; the fewer obstacles the interface encounters, the more domain growth; the more domain growth, the more surface obstacles dominate the response, and the more energy dissipated per unit volume. This line of reasoning assumes that there is a homogeneous distribution of obstacles that will be sampled in an average sense by the transformation. However, a natural extension of this view is that for samples at the finest scales, the transformation may encounter obstacles only rarely and stochastically, so a description based on average encounters is no longer applicable. This idea, that the scarcity of defects may control behavior of small scale martensitic materials has been used in explaining the loss of martensite formation [12, 70, 71]. In these cases, defects are not treated as 'obstacles' to transformation front motion, but as potential nuclei for the initiation of the transformation in the first place. For example, the suppression of martensite in Fe-Ni beads in the micron range was attributed to the small probability of finding a defect with high enough nucleation potency in small beads [70]. Statistical models taking advantage of a Poisson type probability distribution of defects describe such trends well and show that nucleation is heterogeneous: it preferentially occurs on crystallographic defects [70, 71].

Using the density definitions from Section 4 in a grain of aspect ratio 4 ($L = 4 \cdot D$), the most probable number of defects, N, is

$$N = \pi \cdot n_v \cdot D^3 (1 + \frac{4 \cdot D_o}{D}) \quad (3)$$

and the probability of having at least one such defect at the austenite/martensite interface is

$$P = 1 - e^{-N} \quad (4)$$

If we use the values for obstacle density and obstacle size determined earlier, starvation of nucleation sites/obstacles will start to become important for characteristic sizes of a few microns, e.g., P = 0.5 when D = 4.6 μm. This is in line with previous studies on martensite suppression that also commence for characteristic lengths of some microns [12, 70, 72] and it implies that another cross-over may be expected at finer scales than studied in the present experiments: from surface to obstacle starvation-controlled behavior.

If we combine the probability of encountering an obstacle (Eq. 4) with Eq. 2, the 'stochastic' hysteresis size, $\Delta\sigma_s$, now becomes

$$\Delta\sigma_s = E_0 \cdot n_v (1 + \frac{4 \cdot D_o}{D}) \cdot (1 - e^{-\pi \cdot n_v \cdot D^3 (1 + \frac{4 \cdot D_o}{D})}) \quad (5)$$

In Fig. 7 we plot $\Delta\sigma_s$ against sample diameter for all the data from Fig. 6, together with data from small pillars of Cu-Al-Ni [17, 18, 20] and Ni-Mn-Ga (curves exhibiting the largest recoverable strain without residual strain are used) [8]. For diameters above roughly 10 μm the model is the same as that in Fig. 6. For samples smaller than that, the hysteresis rise from increasing surface-to-volume ratio is countered by a decreasing probability of encountering obstacles. Because the starvation term has square and cubic dependencies on D this results in a drop in hysteresis size below about 10 μm. For sample dimensions below 100 nm the

hysteresis becomes vanishingly small. We note that as compared to Fig. 6, the analysis in Fig. 7 requires no additional adjustable parameters to be fitted; the cross-over to defect starvation, reflecting that the Poisson term becomes dominant in Eq. 5, emerges at approximately the correct location (at ~6 μm) based only on our earlier analysis of defect density and spacing. The data in the starvation-dominated regime is taken from very different sample types and alloys and the discrepancy between data and model in Fig. 7 is therefore likely related to those samples having different values of n_v, and D_0.

The schematization of three distinct regimes in Fig. 7 is physically reasonable in light of the body of experimental observations. The addition of the starvation-dominated regime reflects the decreased probability of encountering microstructural defects and therefore also the decreased nucleation probability. In the absence of suitable nucleation defects austenite will be stable at all - or at least a wider range of - temperatures, as has been reported in many recent studies on nanometer scale SMAs [3, 9, 10, 12, 73]. The onset of this regime depends not only on size but also on defect density, which may explain the large range of critical sizes reported for martensite suppression in samples obtained through different processing routes [3, 9, 10, 12, 73].

7. Conclusions

The morphology of Cu-Zn-Al microwires during a superelastic cycle has been studied by *in situ* scanning electron microscopy deformation experiments. To our knowledge this is the first systematic study of superelastic transformation morphology in the size range of ~20 to ~130 μm. A transition from multi-domain to single-domain transformation morphology is observed as the wire diameter is decreased. We relate the transition from a nucleation-dominated to a monolithic morphology to the ease of

domain growth: the fewer obstacles the interface encounters, the more domain growth. Furthermore, we use our observations to rationalize observed sample size effects upon transformation hysteresis in shape memory alloys based on the frictional energy dissipated when obstacles are bypassed by the austenite/martensite interface: the smaller the wire, the more obstacles are sampled on a per volume basis, and the larger the hysteresis size.

Acknowledgements

This work was supported by the US Office of Army Research, through the Institute for Soldier Nanotechnologies at MIT.

[1] Waitz T, Antretter T, Fischer FD, Simha NK, Karnthaler HP. J Mech Phys Solids 2007;55:419.
[2] Dunand DC, Mullner P. Adv Mater 2011;23:216.
[3] Fu YQ, Zhang S, Wu MJ, Huang WM, Du HJ, Luo JK, Flewitt AJ, Milne WI. Thin Solid Films 2006;515:80.
[4] Busch JD, Johnson AD, Lee CH, Stevenson DA. J Appl Phys 1990;68:6224.
[5] Phillips FR, Fang D, Zheng HX, Lagoudas DC. Acta Mater 2011;59:1871.
[6] Frick CP, Orso S, Arzt E. Acta Mater 2007;55:3845.
[7] Clark BG, Gianola DS, Kraft O, Frick CP. Adv Eng Mater 2010;12:808.
[8] Ozdemir N, Karaman I, Mara NA, Chumlyakov YI, Karaca HE. Acta Mater 2012;60:5670.
[9] Ishida A, Sato M. Acta Mater 2003;51:5571.
[10] Waitz T, Kazykhanov V, Karnthaler HP. Acta Mater 2004;52:137.
[11] Waitz T, Tsuchiya K, Antretter T, Fischer FD. Mrs Bull 2009;34:814.
[12] Cech RE, Turnbull D. T Am I Min Met Eng 1956;206:124.
[13] Chmielus M, Zhang XX, Witherspoon C, Dunand DC, Mullner P. Nat Mater 2009;8:863.
[14] Ueland SM, Chen Y, Schuh CA. Adv Funct Mater 2012;22:2094.
[15] Ueland SM, Schuh CA. Acta Mater 2012;60:282.
[16] Chen Y, Schuh CA. Acta Mater 2011;59:537.
[17] Juan JMS, No ML, Schuh CA. Adv Mater 2008;20:272.
[18] Juan JS, No ML, Schuh CA. Nat Nanotechnol 2009;4:415.
[19] Juan JS, No ML, Schuh CA. J Mater Res 2011;26:2461.
[20] San Juan J, No ML, Schuh CA. Acta Mater 2012;60:4093.
[21] Wollants P, Roos JR, Delaey L. Prog Mater Sci 1993;37:227.
[22] Ortin J, Planes A. Acta Metall Mater 1988;36:1873.
[23] Qiao L, Rimoli JJ, Chen Y, Schuh CA, Radovitzky R. Phys Rev Lett 2011;106.
[24] Brinson LC, Schmidt I, Lammering R. J Intel Mat Syst Str 2002;13:761.
[25] Brinson LC, Schmidt I, Lammering R. J Mech Phys Solids 2004;52:1549.
[26] Li ZQ, Sun QP. Int J Plasticity 2002;18:1481.
[27] Shaw JA, Kyriakides S. Int J Plasticity 1997;13:837.
[28] Fang DN, Lu W, Hwang KC. Metall Mater Trans A 1999;30:1933.

[29] Daly S, Miller A, Ravichandran G, Bhattacharya K. Acta Mater 2007;55:6322.
[30] Daly S, Ravichandran G, Bhattacharya K. Acta Mater 2007;55:3593.
[31] Lackmann J, Niendorf T, Maxisch M, Grundmeier G, Maier HJ. Mater Charact 2011;62:298.
[32] Favier D, Louche H, Schlosser P, Orgeas L, Vacher P, Debove L. Acta Mater 2007;55:5310.
[33] Zhang XH, Feng P, He YJ, Yu TX, Sun QP. Int J Mech Sci 2010;52:1660.
[34] He YJ, Sun QP. Int J Solids Struct 2009;46:3045.
[35] Otsuka K, Wayman CM, Nakai K, Sakamoto H, Shimizu K. Acta Metall Mater 1976;24:207.
[36] Ye J, Mishra RK, Pelton AR, Minor AM. Acta Mater 2010;58:490.
[37] Ibarra A, Caillard D, San Juan J, No ML. Appl Phys Lett 2007;90.
[38] Zarubova N, Ge Y, Gemperlova J, Gemperle A, Hannula SP. Funct Mater Lett 2012;5.
[39] Dlouhy A, Khalil-Allafi J, Eggeler G. Philos Mag 2003;83:339.
[40] Michutta J, Somsen C, Yawny A, Dlouhy A, Eggeler G. Acta Mater 2006;54:3525.
[41] Bataillard L, Bidaux JE, Gotthard R. Philos Mag A 1998;78:327.
[42] Shi H, Pourbabak S, van Humbeeck J, Schryvers D. Scripta Mater 2012;67:939.
[43] Zheng HX, Luo ZP, Fang D, Phillips FR, Lagoudas DC. Mater Lett 2012;70:109.
[44] No ML, Ibarra A, Caillard D, Juan JS. Acta Mater 2010;58:6181.
[45] No ML, Calliard D, San Juan J. Acta Mater 2009;57:1004.
[46] Manchuraju S, Kroeger A, Somsen C, Dlouhy A, Eggeler G, Sarosi PM, Anderson PM, Mills MJ. Acta Mater 2012;60:2770.
[47] Tian HF, Lu JB, Ma L, Shi HL, Yang HX, Wu GH, Li JQ. J Appl Phys 2012;112.
[48] Ibarra A, San Juan J, Bocanegra EH, Caillard D, No ML. Mat Sci Eng a-Struct 2006;438:787.
[49] Simon T, Kroger A, Somsen C, Dlouhy A, Eggeler G. Acta Mater 2010;58:1850.
[50] Kumar DMR, Rao DVS, Rao NVR, Raja MM, Singh RK, Suresh KG. Intermetallics 2012;25:126.
[51] Ibarra A, San Juan J, Bocanegra EH, No ML. Acta Mater 2007;55:4789.
[52] Taylor GF. Phys Rev 1924;23:655.
[53] Donald IW. J Mater Sci 1987;22:2661.
[54] Chen Y, Zhang XX, Dunand DC, Schuh CA. Appl Phys Lett 2009;95.
[55] Online supplemental material for this article.
[56] Lovey FC, Isalgue A, V T. Acta Metallurgica Et Materialia 1992;40:3389.
[57] Amengual A, Torra V. Thermochim Acta 1992;198:381.
[58] Lovey FC, Amengual A, Torra V, Ahlers M. Philos Mag A 1990;61:159.
[59] Li HJ, Dunne D, Kennon N. Mat Sci Eng a-Struct 1999;273:517.
[60] Adnyana DN. Metallography 1986;19:187.
[61] Brofman PJ, Ansell GS. Metall Trans A 1983;14:1929.
[62] Delcastillo CL, Mellor BG, Blazquez ML, Gomez C. Scripta Metall Mater 1987;21:1711.
[63] Seki K, Kura H, Sato T, Taniyama T. J Appl Phys 2008;103.
[64] Umemoto M, Owen WS. Metall Trans 1974;5:2041.
[65] Mukunthan K, Brown LC. Metall Trans A 1988;19:2921.
[66] Lovey FC, Torra V. Prog Mater Sci 1999;44:189.
[67] Van Humbeeck J, Kustov S. Smart Mater Struct 2005;14:S171.
[68] Sutou Y, Omori T, Yamauchi K, Ono N, Kainuma R, Ishida K. Acta Mater 2005;53:4121.
[69] Vives E, Burrows S, Edwards RS, Dixon S, Manosa L, Planes A, Romero R. Appl Phys Lett 2011;98.
[70] Chen IW, Chiao YH, Tsuzaki K. Acta Metall Mater 1985;33:1847.

[71] Cohen M. Mater T Jim 1992;33:178.
[72] Heuer AH, Claussen N, Kriven WM, Ruhle M. J Am Ceram Soc 1982;65:642.
[73] Fu YQ, Shearwood C. Scripta Mater 2004;50:319.

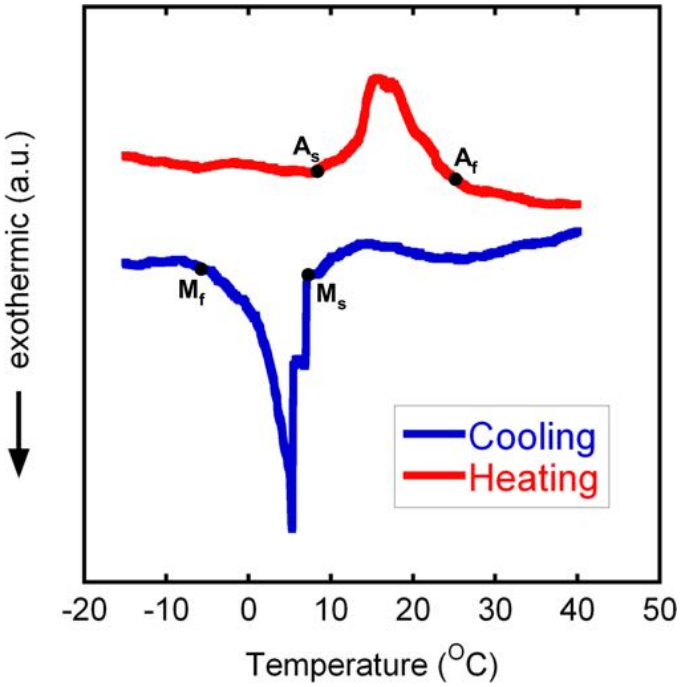

Figure 1. Heating and cooling differential scanning calorimetry (DSC) curves of Cu-Zn-Al microwire with diameter of 65 µm showing transformation temperatures.

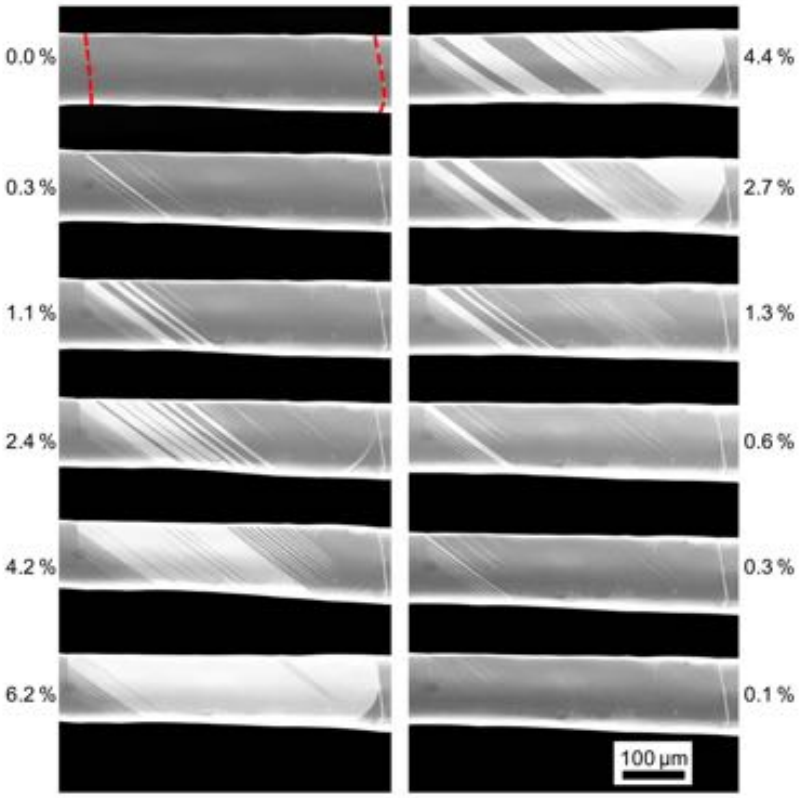

Figure 2. *In situ* scanning electron microscopy images showing the evolution of martensite morphology during a superelastic cycle at room temperature. The wire is Cu-Zn-Al with a diameter of 116 μm and the dashed red lines mark grain boundary locations. Images from loading are on the left and unloading are on the right. The contrast of the martensite phase has been enhanced for visual clarity.

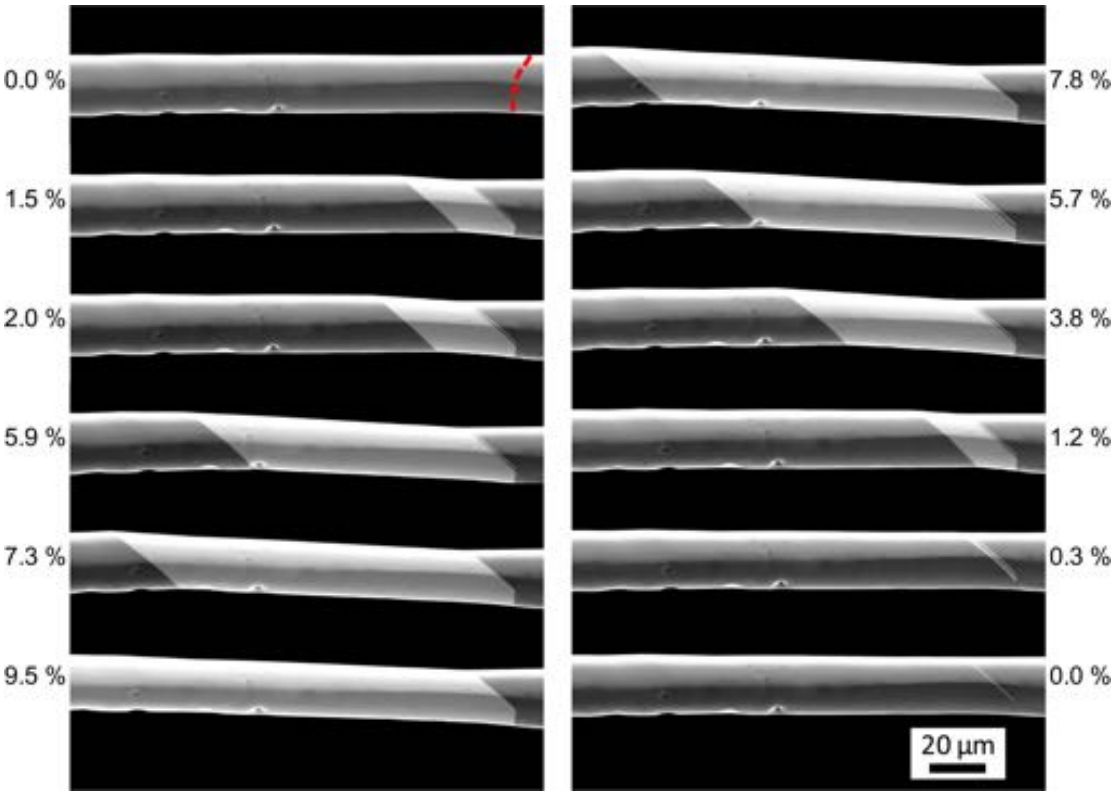

Figure 3. *In situ* scanning electron microscopy images showing the evolution of martensite morphology during a superelastic cycle at room temperature. The wire is Cu-Zn-Al with a diameter of 21 μm and the dashed red line marks a grain boundary location. Images from loading are on the left and unloading are on the right. The contrast of the martensite phase has been enhanced for visual clarity.

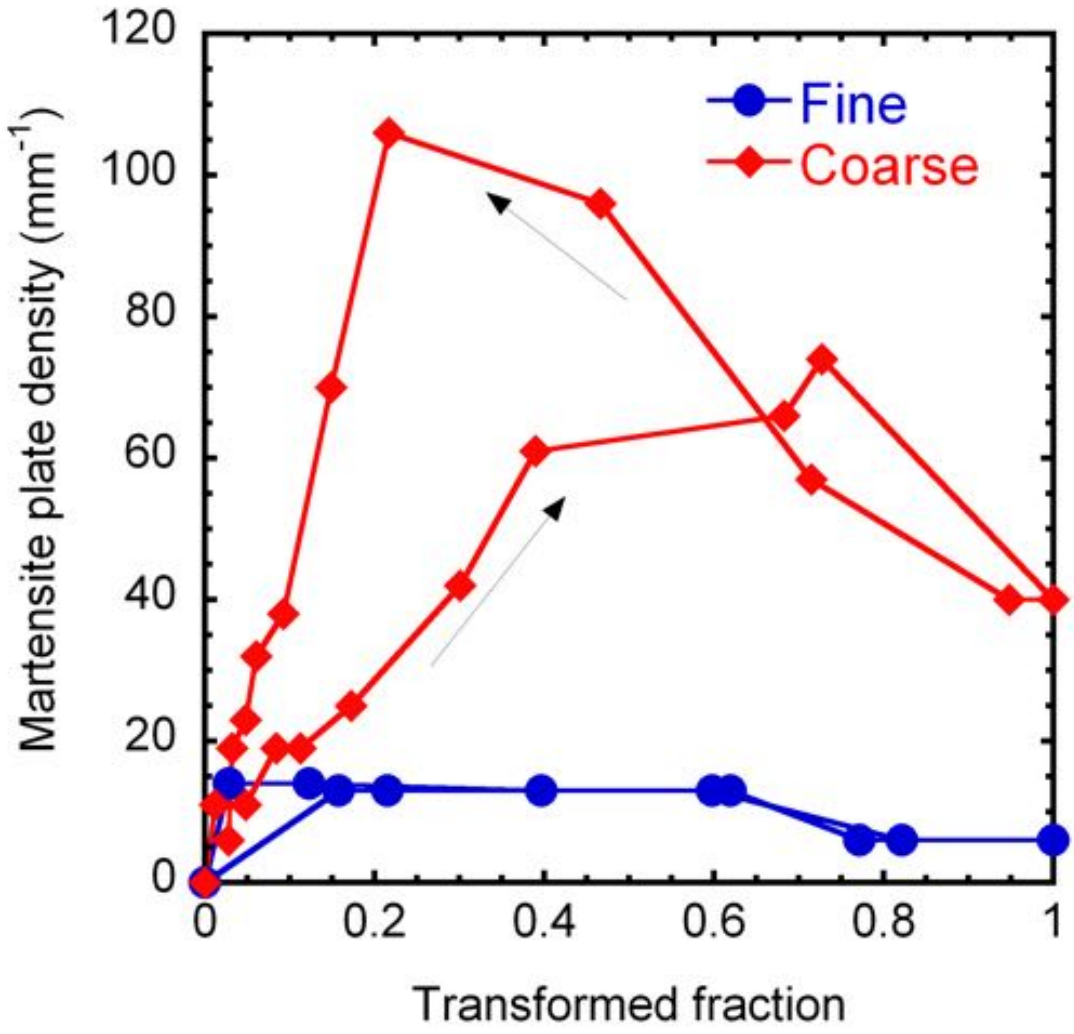

Figure 4. Number of martensite plates per unit length of wire for the fine wire (blue circles) and the coarser wire (red squares) during a full superelastic cycle plotted against transformed fraction (martensite volume fraction). Arrows indicate loading and unloading.

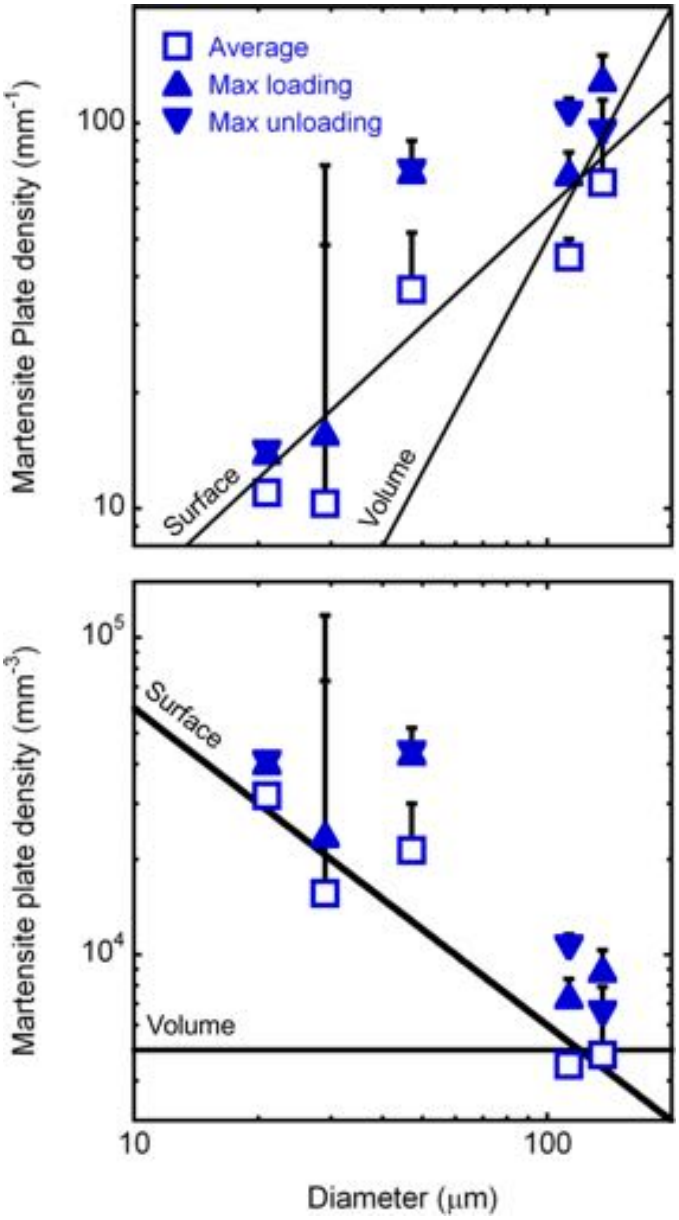

Figure 5. (a) Linear and (b) volumetric martensite plate density (maximum upon loading, maximum upon unloading and average for all the acquired images) plotted against wire diameter for five different samples. The lines represent scaling relationships expected for surface and volume obstacles.

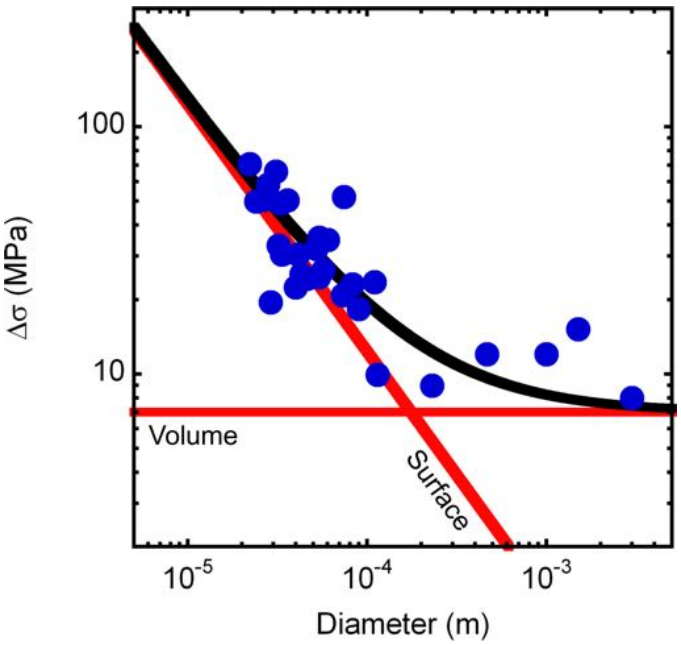

Figure 6. Stress hysteresis plotted against sample diameter for Cu-based shape memory alloys. Blue circles with diameters below 300 μm are Cu-Zn-Al and Cu-Al-Ni microwires. Blue circles with diameters larger than 300 μm are large single crystalline Cu-based SMAs [35, 68, 69]. Details of experimental data can be found in Ref [14]. The black curve is Eq. 2 and the red curves are the surface and volume terms of Eq. 2 plotted separately.

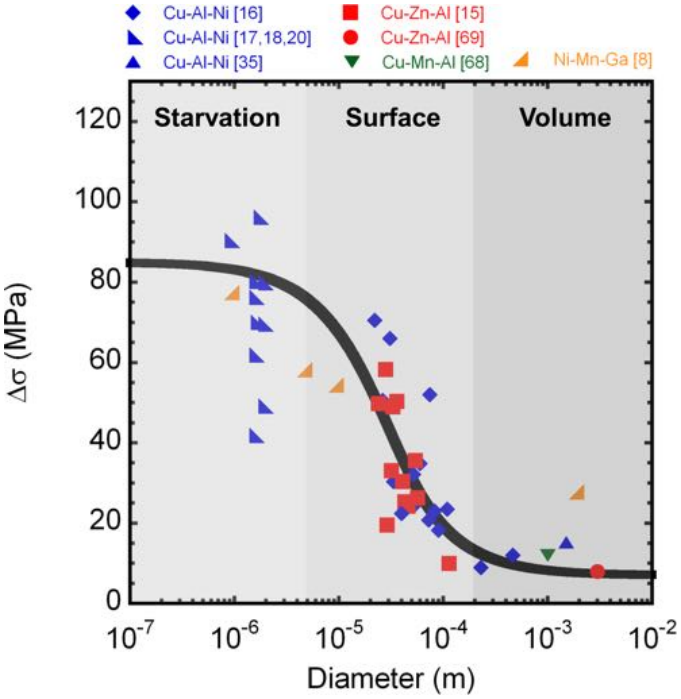

Figure 7. Stress hysteresis plotted against sample diameter. Colors indicate alloy family and the black curve is a model for hysteresis size developed in the text (Eq. 5). All data points are from superelastic curves where the reversible strain is above 3 % and without any residual deformation. Three regimes are distinguished where hysteresis size is dominated by different terms in Eq. 5.